



# High combustion activity of CH<sub>4</sub> and catalluminescence properties of CO oxidation over porous Co<sub>3</sub>O<sub>4</sub> nanorods

Fei Teng<sup>a,\*</sup>, Mindong Chen<sup>a,\*</sup>, Guiqing Li<sup>a</sup>, Yang Teng<sup>b</sup>, Tongguang Xu<sup>c</sup>, Yechao Hang<sup>a</sup>, Wenqing Yao<sup>d</sup>, Sunand Santhanagopalan<sup>e</sup>, Dennis Desheng Meng<sup>e</sup>, Yongfa Zhu<sup>d,\*</sup>

<sup>a</sup> Jiangsu Key Laboratory of Atmospheric Environment Monitoring and Pollution Control, Innovative Research Laboratory of Clean Energy, Environmental Catalysis & New Materials, School of Environmental Science and Engineering, Nanjing University of Information Science & Technology, 219 Ningliu Road, Nanjing 210044, China

<sup>b</sup> Department of Information Science, Suzhou Institute of Trade and Commerce, Suzhou 215009, China

<sup>c</sup> Department of Chemistry, Tsinghua University, Beijing 100086, China

<sup>d</sup> Beijing Cigarette Factory, Beijing 101121, China

<sup>e</sup> Department of Mechanical Engineering-Engineering Mechanics, Michigan Technological University, Houghton, MI 49931, USA

## ARTICLE INFO

### Article history:

Received 29 April 2011

Received in revised form 24 August 2011

Accepted 26 August 2011

Available online 3 September 2011

### Keywords:

Porous nanorods

Catalluminescence

Catalytic oxidation, High gas hourly space velocity

## ABSTRACT

The highly porous Co<sub>3</sub>O<sub>4</sub> nanorods are prepared by a simple hydrothermal method, in which CO(NH<sub>2</sub>)<sub>2</sub> is employed as precipitating agent, and K60 (PVP, polyvinylpyrrolidone) is used as surfactant to improve the stability of the nanoparticles. For comparison, the bulk Co<sub>3</sub>O<sub>4</sub> is prepared by thermal decomposition of cobalt nitrate. The samples are characterized by field emission scanning electron microscopy (FE-SEM), energy dispersive X-ray spectroscopy (EDX), X-ray diffraction (XRD), high-resolution transmission electron microscopy (HRTEM), selected area electron diffraction (ED), X-ray photoelectron spectroscopy (XPS), Raman spectroscopy, N<sub>2</sub> adsorption, Thermogravimetric analysis (TG), H<sub>2</sub>-temperature programmed reduction (TPR), CO-, CH<sub>4</sub>-, and O<sub>2</sub>-temperature programmed desorption (TPD). The catalluminescence (CTL) and catalytic properties of the samples are investigated extensively. The results show that the Co<sub>3</sub>O<sub>4</sub> nanorods are composed of nanoparticles, and have a large number of pores with a narrow pore size distribution (1.5–7 nm). Compared with the bulk Co<sub>3</sub>O<sub>4</sub>, the porous nanorods have a higher CTL intensity of CO oxidation, and a higher activity of CH<sub>4</sub> combustion especially at a higher gas hourly space velocity (GHSV), which has been ascribed to its porous structure and larger surface area.

© 2011 Elsevier B.V. All rights reserved.

## 1. Introduction

The physicochemical properties of the materials are strongly dependent on their compositions, intrinsic crystal structures, morphologies and microstructures [1–3]. Thus, considerable efforts have been performed to design various micro/nanostructures. Recently, the porous inorganic materials have attracted great interest because of their wide applications in lithium-ion batteries [4] and catalysis [5]. For a porous material, the catalytic reaction cannot only occur on the outside surface, but also throughout the inner surface [6]. For power generation of natural gas, the high gas-hourly-space-velocity (GHSV) feeds are generally exploited. Although many catalysts exhibit the high activities at low GHSV feeds, their activities at high GHSV feeds are often unfavorable due to the limitation by mass transportation. Although the activities

of the catalysts can be improved by the uses of high-surface-area supports, but it is inevitable to increase the complications of the preparation procedures. Hence it is still a big challenge to develop the excellent catalysts at the high GHSV feeds.

As an important p-type semiconductor, Co<sub>3</sub>O<sub>4</sub> has received a significant attention [7–27]. Mesoporous Co<sub>3</sub>O<sub>4</sub> has successfully been prepared by employing ordered mesoporous silica materials (e.g., MCM41, SBA-15 and KIT-6) as templates [19,21,24]. It is found that these mesoporous Co<sub>3</sub>O<sub>4</sub> samples have the improved rate capability and cycling life for lithium-ion batteries [23]. Nevertheless, the yields of the products are generally limited by the used amounts of templates and this preparation approach is generally complicate and expensive. It is desirable to develop a facile method to synthesize the porous Co<sub>3</sub>O<sub>4</sub> and to explore their catalytic properties different from the solid structure.

In this work, the porous Co<sub>3</sub>O<sub>4</sub> nanorods with a narrow pore-size distribution and the bulk Co<sub>3</sub>O<sub>4</sub> are synthesized by the hydrothermal and the thermal decomposition methods, respectively. The samples are characterized by field emission scanning electron microscopy (FE-SEM), energy dispersive X-ray spectroscopy (EDX),

\* Corresponding authors. Tel.: +86 25 98738888; fax: +86 25 98738888.

E-mail addresses: 001880@nuist.edu.cn (F. Teng), chenmdnj@nuist.edu.cn (M. Chen), zhuyf@tsinghua.edu.cn (Y. Zhu).

X-ray diffraction (XRD), high-resolution transmission electron microscopy (HRTEM), selected area electron diffraction (ED), X-ray photoelectron spectroscopy (XPS), Raman spectroscopy, N<sub>2</sub> adsorption, Thermogravimetric analysis (TG), H<sub>2</sub>-temperature programmed reduction (TPR), CO-, CH<sub>4</sub>-, and O<sub>2</sub>-temperature programmed desorption (TPD). Moreover, their catalytic activities of CH<sub>4</sub> combustion at the different GHSV feeds, as well as their catalluminescence (CTL) properties of CO oxidation, are mainly investigated. The main aim of our study is to develop the excellent Co<sub>3</sub>O<sub>4</sub> catalysts at the high GHSV feeds.

## 2. Experimental

### 2.1. Preparation of the porous sample

In the experiment, all the chemicals are of analytic grade and purchased from Beijing Chemicals Company, which are used without further purification.

The porous Co<sub>3</sub>O<sub>4</sub> nanorods are synthesized under hydrothermal conditions. Typically, 0.003 mole CoCl<sub>2</sub>·6H<sub>2</sub>O, 0.018 mole CO(NH<sub>2</sub>)<sub>2</sub> and 15 g of 35 wt% K60 aqueous solution (PVP, polyvinylpyrrolidone, molecular weight = 200,000) are dissolved in 25 mL deionized water under stirring to form a clear solution. The solution is transferred into a 50 mL Teflon®-lined stainless steel autoclave, and then is heated to 90 °C and kept at this temperature for 24 h. After being cooled naturally to room temperature, the sample is centrifuged, washed with DI water and ethanol for three times, respectively. Finally, the sample is dried at 80 °C for 24 h in a vacuum oven. Under a flow of air, the product is obtained by further calcination at 400 °C for 3 h at a ramping rate of 1 °C min<sup>-1</sup>. For comparison, the bulk Co<sub>3</sub>O<sub>4</sub> sample is prepared by the thermal decomposition of Co(NO<sub>3</sub>)<sub>3</sub> at 700 °C for 5 h in air. The samples are characterized by FE-SEM, EDX, HRTEM, ED, XRD, XPS, Raman spectroscopy, TG, N<sub>2</sub> adsorption, H<sub>2</sub>-TPR, CO-, O<sub>2</sub>- and CH<sub>4</sub>-TPD. The characterization details can be found in supporting information.

#### 2.1.1. The CTL properties

The CTL detection system employed in this work is given in the reference [28]. The detect system consists of a CTL sensor, a digital programmable temperature controller and an optical detector. The CTL sensor is made by sintering a 0.15-mm-thick layer of the catalyst powder (10 ± 0.1 mg, weighed by analysis balance) on a cylindrical ceramic heater of 5 mm in diameter. Typically, 0.01 g of the powders are mixed with absolute ethanol to prepare a paste, and the paste is coated on the surface of heating tube; then it is kept at 110 °C for 24 h and at 200 °C for 1 h in air to form a coating. In order to accurately control the thickness, the same procedure is repeated for 3 times. The weight difference of the coating is controlled within ±0.5%. The obtained sensor is set in a quartz tube of 12-mm (i.d.), through which an air at atmospheric pressure flows at a constant rate. A certain volume pulse of CO is injected into the flow of air. The reaction gases can only flow through the outside of solid ceramic heater. A digital temperature controller is used to control the temperatures of the sensor. The CTL intensity at a certain wavelength is measured by a photon-counting method with a BPCL ultraweak luminescence analyzer (BPCL, catalluminescence analyzer made by Biophysics Institute of the Chinese Academy of Science). In the experiment, the optical filter with the wavelength of 620 nm is used. Before each test, the sensor is heated at 200 °C for 0.5 h in air to eliminate the previous absorbates.

#### 2.1.2. Catalytic oxidation of CO

The oxidation reaction of CO is carried out in a conventional flow system at atmospheric pressure. 1 mL of the sample (20–40 mesh) is loaded in a quartz reactor (inner diameter: 5 mm), with

quartz beads packed at both ends of the catalyst bed. The thermal couple is inserted into the catalyst bed to monitor the reaction temperature. Before each run, the catalyst is flushed with air at 300 °C for 1 h to remove the previous absorbates from the catalyst surface, and then cooled to 30 °C. The mixed gases of 1 vol.% CO and 99 vol.% air are fed into the catalyst bed at a gas hourly space velocity (GHSV) of 12,000 or 36,000 h<sup>-1</sup>. The compositions of the inlet and outlet gases are analyzed by an on-line gas chromatograph with a GDX-403 GC-column (1.5 m × 4 mm) at 100 °C and a hydrogen flame ionization detector (FID). Herein, the temperatures at 10% and 100% conversions of CO are designated as *T*<sub>10</sub> and *T*<sub>100</sub>, respectively.

#### 2.1.3. Catalytic combustion of CH<sub>4</sub>

The combustion of CH<sub>4</sub> is conducted in a conventional flow system at atmospheric pressure. First, 1 mL of the sample (20–40 mesh) is diluted with 1 mL of quartz powder and loaded into a quartz reactor (5 mm i.d.) with quartz beads packed at both ends of the catalyst bed. The thermocouple is placed in the catalyst bed to monitor the reaction temperature, because CH<sub>4</sub> oxidation is an exothermic reaction. Before each run, the catalyst is flushed with 100 mL min<sup>-1</sup> air at 300 °C for 1 h to remove adsorbed species from the surface, and then cooled to 50 °C. A gas mixture of 2 vol.% CH<sub>4</sub> and 98 vol.% air is fed into the catalyst bed at a GHSV of 48,000 or 100,000 h<sup>-1</sup>. The compositions of the inlet and outlet gases are analyzed by an online GC with a packed column of carbon molecular sieve (1.5 m × 4 mm) and a TCD. Herein, the temperatures at 10% and 90% conversions of CH<sub>4</sub> are designated as *T*<sub>10</sub> and *T*<sub>90</sub>, respectively.

## 3. Results

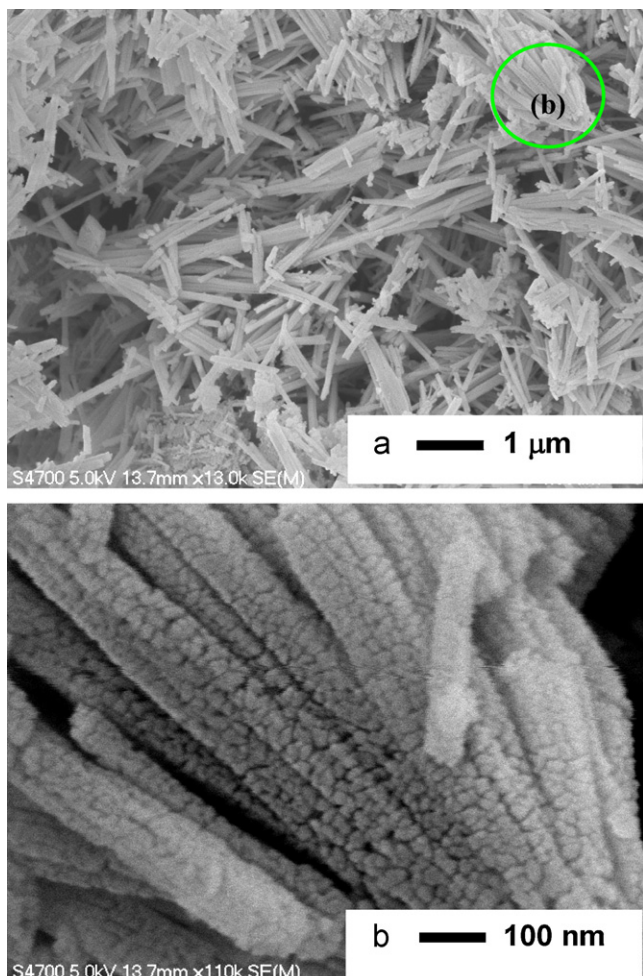
### 3.1.1. Microstructure and textural properties of the porous nanorods

Fig. 1 shows the typical FE-SEM images of the as-obtained sample. At a low magnification (Fig. 1a), a large number of Co<sub>3</sub>O<sub>4</sub> nanorods can be observed, which have the diameter of 50–100 nm and the length of 1–4 μm. At a high magnification (Fig. 1b), these Co<sub>3</sub>O<sub>4</sub> nanorods are not solid monoliths, but consist of about 10 nm nanoparticles. The weight ratio of O(K) to Co(K) is determined to be 9.49:90.51 by EDX (Fig. S1 of supporting information). The results of XPS and Raman spectroscopy also demonstrate the formation of the pure Co<sub>3</sub>O<sub>4</sub> crystals (Figs. S2 and S3 of supporting information). Fig. 2 shows the XRD patterns of the samples. All the diffraction peaks of both samples can be well indexed as the pure Co<sub>3</sub>O<sub>4</sub> spinel with a lattice constant of *a* = 0.8084 nm (space group: *Fd*3*m*), which is in agreement with the reported values (JCPDS No. 42-1467) [29,30]. The mean sizes (*D*) of the nanocrystallites are estimated using the Debye–Scherrer formula [31]:

$$D = \frac{k\lambda}{(\beta \cos \theta)} \quad (1)$$

where *k* is a constant (0.89), *λ* is the X-ray wavelength, *β* is the full width at half maximum of the diffraction peak and *θ* is the Bragg diffraction angle. On base of (111) peak, the mean crystal sizes of the porous and the bulk samples are calculated to be 10.5 and 45.5 nm, respectively.

Fig. 3a shows that the Co<sub>3</sub>O<sub>4</sub> nanorods consist of about 10-nm nanoparticles, which is consistent with the FE-SEM results. The bright-dark contrast indicates that these nanoparticles have not formed solid monoliths. The porous nature of the Co<sub>3</sub>O<sub>4</sub> nanorods can be proven at a high magnification. In Fig. 3b, a pore of about 4 nm is observed through the bright-dark contrast. The lattice fringe spacings are determined to be 0.467 and 0.286 nm, corresponding to the (111) and (220) planes of the Co<sub>3</sub>O<sub>4</sub> crystals. Fig. 3c



**Fig. 1.** FE-SEM images of the porous  $\text{Co}_3\text{O}_4$  sample at (a) low and (b) high magnifications.

shows the ED patterns of the sample, the interplanar distances are calculated to be 0.46, 0.28, 0.25, 0.15 and 0.14 nm, corresponding to the (111), (220), (311), (422) and (440) planes. The similar results have been reported by Liu et al. [26]. The results confirm the polycrystalline nature of the nanorods.

In Fig. 4, the  $\text{Co}_3\text{O}_4$  nanorods show an IV-typed sorption isotherm. An H1-typed hysteresis loop appears in the relative pressure range of 0.4–0.7, which may result from the packing of nearly uniform nanoparticles [32,33]. The pore sizes

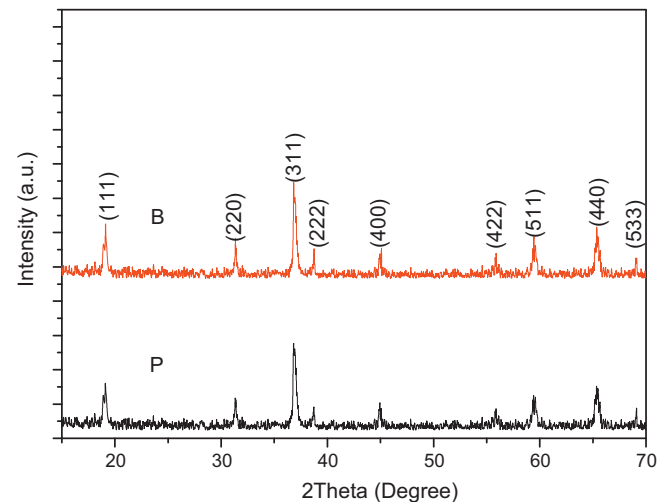


**Fig. 2.** XRD patterns of the  $\text{Co}_3\text{O}_4$  samples: P, Porous nanorods, B, Bulk.

calculated by the Barrett–Joyner–Halenda (BJH) method show a monomodal distribution (centered at 4.2 nm ranging from 2 to 7 nm). The Brunauer–Emmett–Teller (BET) area is determined to be  $170.2 \text{ m}^2 \text{ g}^{-1}$  (Table 2). In Fig. S4 (supporting information), the bulk  $\text{Co}_3\text{O}_4$  sample also shows an IV-typed sorption isotherm. However, an H2-typed hysteresis loop appears in the relative pressure range of 0.8–0.98, which represents a bottleneck packing of non-uniform particles [32,33]. The bulk  $\text{Co}_3\text{O}_4$  sample has a trimodal pore size distribution (centered at 22, 35 and 50 nm in a wide range). The BET area of the bulk  $\text{Co}_3\text{O}_4$  is determined to be  $20.9 \text{ m}^2 \text{ g}^{-1}$ .

To understand the formation of the porous  $\text{Co}_3\text{O}_4$  nanorods, the precursor has been characterized by XRD, FE-SEM and TG (Figs. S5 and S6 of supporting information). According to these results, a probable formation mechanism of the porous  $\text{Co}_3\text{O}_4$  nanorods is proposed (Fig. S7 of supporting information). We could only imagine that the porous  $\text{Co}_3\text{O}_4$  nanorods result from the  $\text{CoCO}_3$  precursor. It is probable that the ferromagnetic moment of  $\text{CoCO}_3$  crystals drive the nanoparticles to form the  $\text{CoCO}_3$  nanorods. In fact, the true formation mechanism needs further studying due to the complication of the reaction.

### 3.1.2. The CTL properties and reaction activities of CO oxidation over the samples

The CTL intensities of CO oxidation over the porous  $\text{Co}_3\text{O}_4$  nanorods at different test temperatures are shown in Fig. 5. While the temperature increases from 140 to 220 °C, the CTL intensity

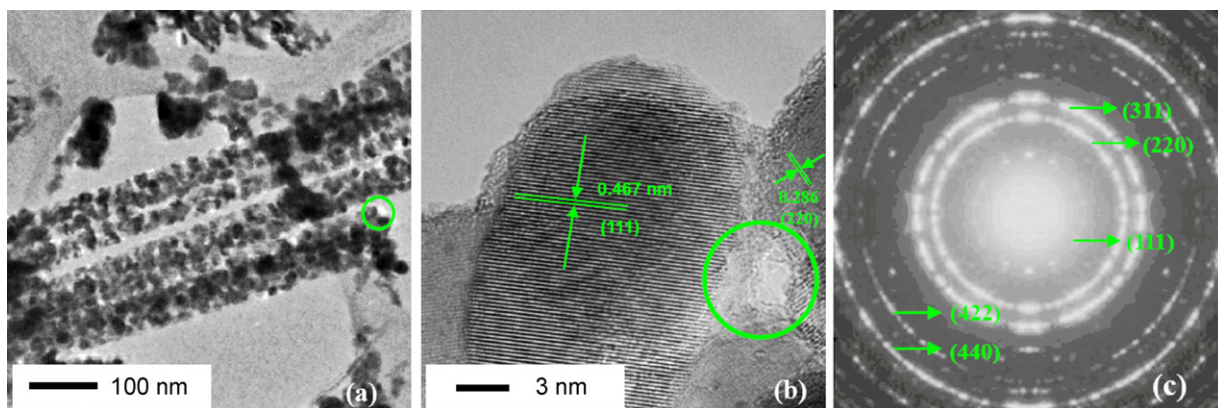


**Fig. 3.** HTEM micrographs of the porous  $\text{Co}_3\text{O}_4$  nanorods: (a) TEM image; (b) Lattice spacing image; (c) ED patterns.

**Table 1**

Analytical characteristics of the cataluminescence (CTL) determination of CO over the  $\text{Co}_3\text{O}_4$  nanorods.

| Linear range ( $C, \mu\text{g mL}^{-1}$ ) | Linear regression equation                        | $R^2$   | Detection limit ( $\mu\text{g mL}^{-1}$ ) |
|---|---|---------|---|
| 5–300                                     | ${}^1I_{\text{CTL}} = A + B \times C_{\text{CO}}$ | 0.99968 | 1.0                                       |

${}^1I_{\text{CTL}}$ , CTL intensity;  $C_{\text{CO}}$ , CO concentration;  $A = 98.10658$ , Error ( $A$ ) = 229.394;  $B = 228.82615$ , Error ( $B$ ) = 1.336;  $R^2$ , Correlative coefficient.

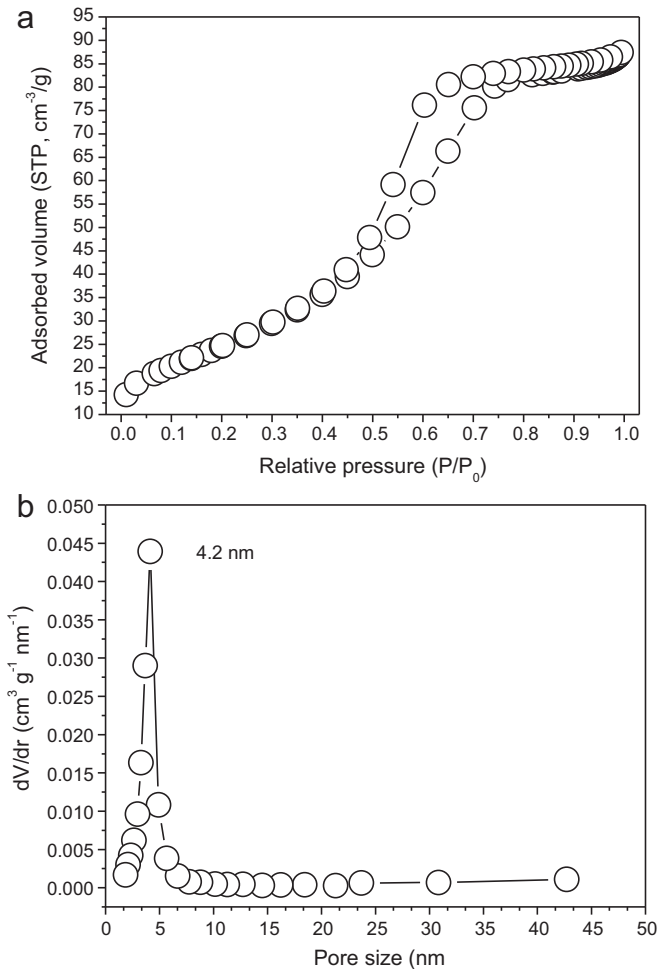


Fig. 4.  $\text{N}_2$  adsorption isotherms (a) and pore size distributions (b) of the porous  $\text{Co}_3\text{O}_4$  sample.

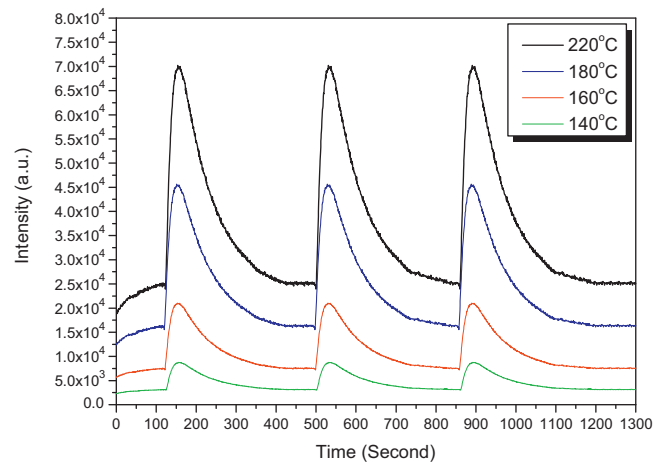


Fig. 5. The CTL spectra of CO oxidation over the porous  $\text{Co}_3\text{O}_4$  nanorods at different temperatures:  $F$  (flowing rate of gas) = 200  $\text{mL min}^{-1}$ ;  $C_{\text{CO}}$  (CO concentration) = 200  $\mu\text{g mL}^{-1}$ ,  $\lambda_{\text{filter}}$  (wave number of filter) = 620 nm.

**Table 2**

The texture properties of both samples.

| Samples | Pore volume ( $\text{mL g}^{-1}$ ) | Most probable pore size (nm) | BET area ( $\text{m}^2 \text{ g}^{-1}$ ) |
|---------|------------------------------------|------------------------------|--|
| P       | 0.53                               | 4.2                          | 170.2                                    |
| B       | 0.11                               | 22, 35, 55                   | 20.9                                     |

P, Porous  $\text{Co}_3\text{O}_4$  nanorods; B, Bulk  $\text{Co}_3\text{O}_4$ ; Pore size distribution, calculated by the Barrett-Joyner-Halenda (BJH) method; Surface area, calculated by the Brunauer–Emmett–Teller (BET) method.

increases from  $0.58 \times 10^4$  to  $4.5 \times 10^4$  a.u. It is clear that the test temperature has a significant influence on CTL intensity. This is because the conversion of CO increases with the temperature, and more  $\text{CO}_2$  molecules are formed at higher temperatures. The effect of CO concentration ( $C_{\text{CO}}$ ) on the CTL intensity is investigated (Fig. 6 and Table 1). A good linear correlation between the CTL intensity and CO concentration can be observed in the concentration range of 0–300  $\mu\text{g mL}^{-1}$ . The correlation coefficient ( $R$ ) is 0.99968 and the detection limit of the CTL sensor for CO oxidation is determined as low as 5  $\mu\text{g mL}^{-1}$ . Therefore the CTL properties of the catalyst should be compared at the same test temperature and concentration of CO. Fig. 7 shows the CTL spectra of the porous nanorods and the bulk sample. The CTL intensity of CO oxidation over the porous  $\text{Co}_3\text{O}_4$  nanorods is higher than that over the bulk sample ( $4.5 \times 10^4$  vs.  $1.3 \times 10^4$ ), indicating that more CO molecules are oxidized into  $\text{CO}_2$  molecules over the porous nanorods at the same test conditions.

Fig. 8 shows the reaction activities of CO oxidation over the catalysts. At  $\text{GHSV} = 12,000 \text{ h}^{-1}$ , the complete conversion temperatures ( $T_{100}$ ) of CO over the porous  $\text{Co}_3\text{O}_4$  nanorods and the bulk one are 210 and 245 °C, respectively. At  $\text{GHSV} = 36,000 \text{ h}^{-1}$ , they increased to 265 and 330 °C by 55 and 85 °C, respectively. The porous  $\text{Co}_3\text{O}_4$  nanorods have a higher activity than the bulk  $\text{Co}_3\text{O}_4$  sample. It is clear that the order of reaction activity is well consistent with the CTL order. Moreover, their activity difference ( $\Delta T_{10} = 25^\circ\text{C}$ ) at a higher GHSV is slightly larger than that ( $\Delta T_{10} = 15^\circ\text{C}$ ) at a lower GHSV. However, their activity difference ( $\Delta T_{100} = 65^\circ\text{C}$ ) at a higher

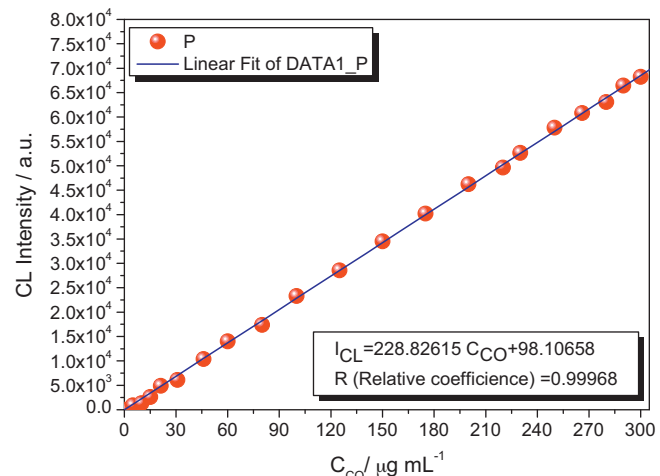
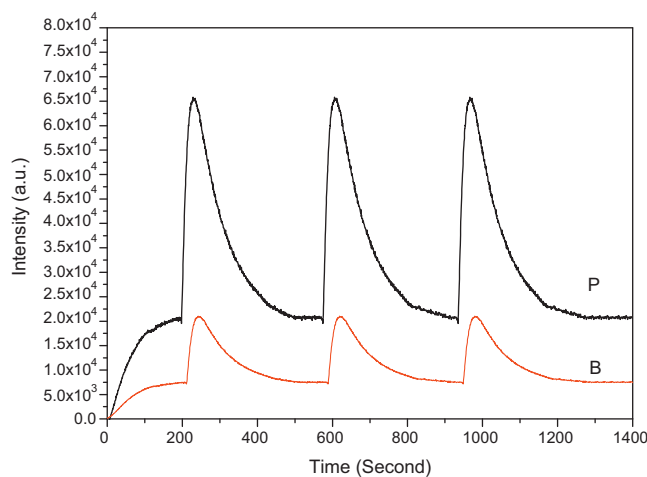
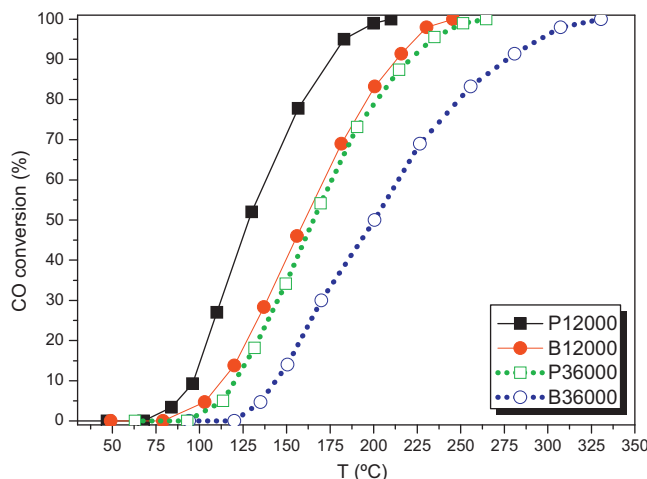


Fig. 6. The intensities of CO oxidation over the porous  $\text{Co}_3\text{O}_4$  nanorods at different  $C_{\text{CO}}$ :  $T = 220^\circ\text{C}$ ,  $F = 200 \text{ mL min}^{-1}$ ,  $\lambda_{\text{filter}} = 620 \text{ nm}$ .



**Fig. 7.** The CTL spectra of CO oxidation over the porous nanorods and the bulk  $\text{Co}_3\text{O}_4$ :  $T=220^\circ\text{C}$ ,  $F=200 \text{ mL min}^{-1}$ ,  $\lambda_{\text{filter}}=620 \text{ nm}$ ,  $C=200 \mu\text{g mL}^{-1}$ .



**Fig. 8.** The activities of CO oxidation over the  $\text{Co}_3\text{O}_4$  samples at different gas hourly space velocities (GHSV): 1 vol.% CO, 99 vol.% air.

GHSV is significantly larger than that ( $\Delta T_{100}=35^\circ\text{C}$ ) at a lower GHSV (Table 3).

### 3.1.3. The combustion activity of $\text{CH}_4$ over the samples

Fig. 9a shows the light-off curves of  $\text{CH}_4$  combustion over the  $\text{Co}_3\text{O}_4$  samples. At GHSV = 48,000  $\text{h}^{-1}$ , the ignition temperature ( $T_{10}$ ) and the complete combustion temperature ( $T_{90}$ ) of the porous  $\text{Co}_3\text{O}_4$  nanorods are 420 and 515 °C, which are 25 and 45 °C lower than those ( $T_{10}=445^\circ\text{C}$ ,  $T_{90}=560^\circ\text{C}$ ) of the bulk sample, respectively. At GHSV = 100,000  $\text{h}^{-1}$ ,  $T_{10}$  and  $T_{90}$  of the porous  $\text{Co}_3\text{O}_4$  nanorods increase by 40 and 45 °C, respectively; but those of the bulk sample increase by 40 and 85 °C, respectively (Table 4).

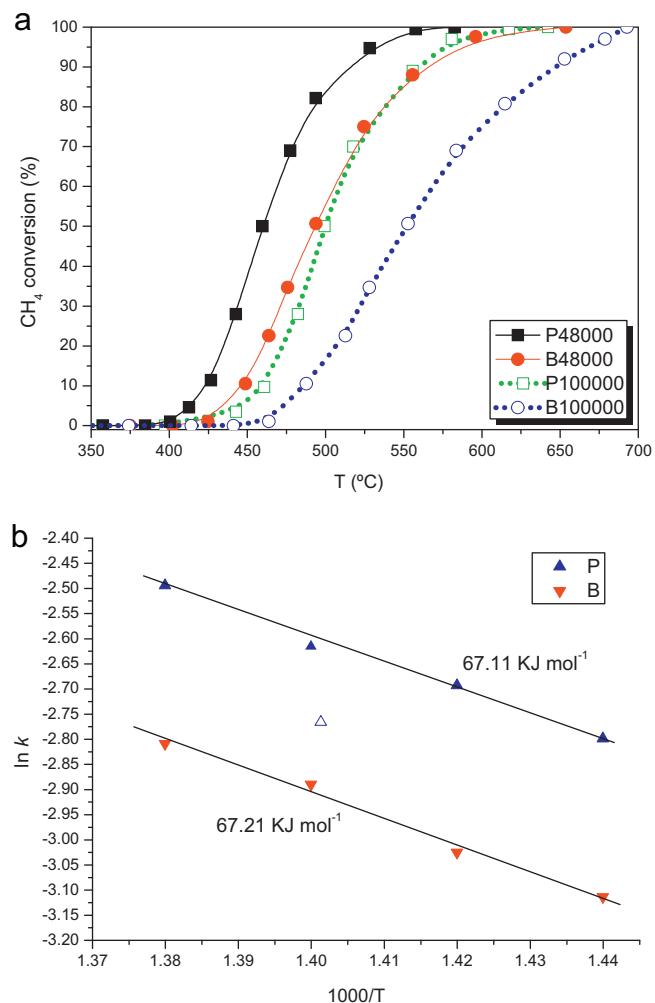


**Fig. 9.** (a) Light-off curves of  $\text{CH}_4$  combustion over the  $\text{Co}_3\text{O}_4$  samples at different GHSVs: 2 vol.%  $\text{CH}_4$ , 98 vol.% air; (b) Arrhenius plots for the reaction rate constants (apparent activation energies,  $E_{\text{app}}$ ) on the samples in the temperature ( $T$ ) range of 420–460 °C with a GHSV = 100,000  $\text{h}^{-1}$ .

It is clear that the activity of the bulk sample decreases more significantly than the porous  $\text{Co}_3\text{O}_4$  nanorods with the increase of GHSV. We have calculated kinetic data to rigorously correlate the reaction activity with physicochemical properties. In the present case, the rate is obtained from below 10% conversions of methane by assuming pseudo-first order kinetics and employing integral mode. Fig. 9b shows the linear Arrhenius plots ( $\ln k$  vs.  $1/T$ ). The deduced apparent activation energies ( $E_{\text{app}}$ ) are 67.11 and 67.21 kJ mole<sup>-1</sup> for the porous and bulk samples, respectively. Considering the experimental error, they have the same  $E_{\text{app}}$  values. The similar values are reported in the literatures [34–37]. Considering the higher BET area and highly porous structure, the porous  $\text{Co}_3\text{O}_4$  nanorods can be used as an excellent catalyst.

**Table 3**

The activities of CO oxidation over the catalysts at different GHSVs.

| Sample | GHSV = 12,000 $\text{h}^{-1}$ |                | GHSV = 36,000 $\text{h}^{-1}$ |                | GHSV = 12,000 $\text{h}^{-1}$ |                       | GHSV = 36,000 $\text{h}^{-1}$ |                       |
|--------|-------------------------------|----------------|-------------------------------|----------------|-------------------------------|-----------------------|-------------------------------|-----------------------|
|        | $T_{10}$ (°C)                 | $T_{100}$ (°C) | $T_{10}$ (°C)                 | $T_{100}$ (°C) | $\Delta T_{10}$ (°C)          | $\Delta T_{100}$ (°C) | $\Delta T_{10}$ (°C)          | $\Delta T_{100}$ (°C) |
| P      | 95                            | 210            | 120                           | 265            |                               |                       |                               |                       |
| B      | 110                           | 245            | 145                           | 330            | 15                            | 35                    | 25                            | 65                    |

GHSV, Gas hourly space velocity;  $T_{10}$ ,  $T_{100}$ ; the temperature at 10% and 100% conversion of CO, respectively;  $\Delta T_{10}$  and  $\Delta T_{100}$ , the temperature difference of porous  $\text{Co}_3\text{O}_4$  nanorods and bulk  $\text{Co}_3\text{O}_4$  at 10% and 100% conversion of CO.

**Table 4**

The activities of  $\text{CH}_4$  combustion over the catalysts at different GHSVs.

| Sample | GHSV = 48,000 $\text{h}^{-1}$   |                                 | GHSV = 100,000 $\text{h}^{-1}$  |                                 | GHSV = 48,000 $\text{h}^{-1}$          |  | GHSV = 100,000 $\text{h}^{-1}$         |  |
|--------|---------------------------------|---------------------------------|---------------------------------|---------------------------------|--|--|--|--|
|        | $T_{10}$ ( $^{\circ}\text{C}$ ) | $T_{90}$ ( $^{\circ}\text{C}$ ) | $T_{10}$ ( $^{\circ}\text{C}$ ) | $T_{90}$ ( $^{\circ}\text{C}$ ) | $\Delta T_{10}$ ( $^{\circ}\text{C}$ ) | $\Delta T_{90}$ ( $^{\circ}\text{C}$ ) | $\Delta T_{10}$ ( $^{\circ}\text{C}$ ) | $\Delta T_{90}$ ( $^{\circ}\text{C}$ ) |
| P      | 420                             | 515                             | 460                             | 560                             | 25                                     | 45                                     | 25                                     | 85                                     |
| B      | 445                             | 560                             | 485                             | 645                             |  |  |  |  |

$T_{10}$  and  $T_{90}$ ; the temperature at 10% and 100% conversion of CO, respectively;  $\Delta T_{10}$  and  $\Delta T_{90}$ , the temperature difference of the porous  $\text{Co}_3\text{O}_4$  nanorods and the bulk  $\text{Co}_3\text{O}_4$ .

**Table 5**

$\text{H}_2$ -TPR peak areas of the  $\text{Co}_3\text{O}_4$  samples.

| Catalyst | Peak area (a.u.)              |                                |                                 | Area ratio of Peak-3 to Peak-2 |
|----------|-------------------------------|--------------------------------|---------------------------------|--------------------------------|
|          | Peak-1                        | Peak-2                         | Peak-3                          |                                |
| P        | 523 (150 $^{\circ}\text{C}$ ) | 7935 (268 $^{\circ}\text{C}$ ) | 23806 (345 $^{\circ}\text{C}$ ) | 3.0111                         |
| B        | 321 (150 $^{\circ}\text{C}$ ) | 7885 (279 $^{\circ}\text{C}$ ) | 23795 (352 $^{\circ}\text{C}$ ) | 3.0103                         |

### 3.1.4. Surface and adsorption properties of the samples

Three reduction peaks can be observed from the  $\text{H}_2$ -TPR profiles of the samples (Fig. 10). According to the literatures [38,39], the first peak at about 150  $^{\circ}\text{C}$  (Peak-1) is attributed to the reduction of surface oxygen species, the second peak at about 200–300  $^{\circ}\text{C}$  (Peak-2) and the third peak at about 300–500  $^{\circ}\text{C}$  (Peak-3) result from the reduction of  $\text{Co}_3\text{O}_4$  to  $\text{CoO}$  and  $\text{CoO}$  to  $\text{Co}$ , respectively (Eq. (2) and (3)).



The chemical equations indicate that the consumed  $\text{H}_2$  mole ratio is 3/1 in both steps. In Table 5, the area ratios of Peak-3 to Peak-2 for both samples are about 3/1, which are quantitatively consistent with the theoretical value. The Peak-1 area over the porous nanorods increases about 3.5% of that over the bulk one, indicating there are more oxygen species on the surface of the former. The Peak-2 and Peak-3 areas over both samples are similar, but their positions over the porous nanorods shift to the lower temperatures (268 and 345), compared with those (279 and 352  $^{\circ}\text{C}$ ) of the bulk sample, respectively. This indicates that the porous nanorods are easier to be reduced than the bulk one, which could be ascribed to the smaller size and the porous structure.

Fig. 11 shows the adsorption behavior of CO molecules on the samples. For the CO adsorption on  $\text{Co}_3\text{O}_4$ , CO molecules attach to the coordination sites of  $\text{CoO}_6$  (unsaturated metal sites,  $\text{Co}^{3+}$ )

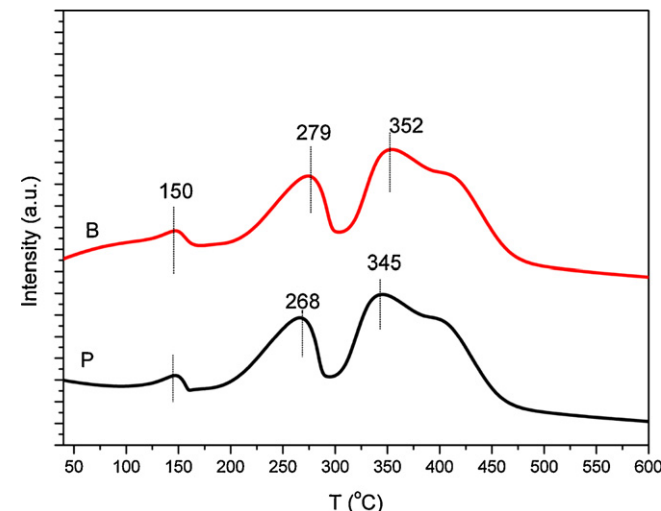


Fig. 10.  $\text{H}_2$ -TPR profiles of the  $\text{Co}_3\text{O}_4$  samples.

where some oxygen ligands are missing. It seems that CO molecules and coordination sites of  $\text{CoO}_6$  function as Lewis bases and acids, respectively. Chemisorption occurs by donation of  $5\sigma$  electrons of CO to Lewis acid sites of  $\text{CoO}_6$ . Since a significant portion of CO molecules desorb in the form of  $\text{CO}_2$  molecules from the catalyst, the total CO adsorption amount on the catalyst is consistent with the total desorption amounts of both  $\text{CO}_2$  and CO molecules. In Fig. 11a, three desorption peaks of CO are observed at about 85, 340 and 350  $^{\circ}\text{C}$  for both catalysts. Fig. 11b shows two obvious desorp-

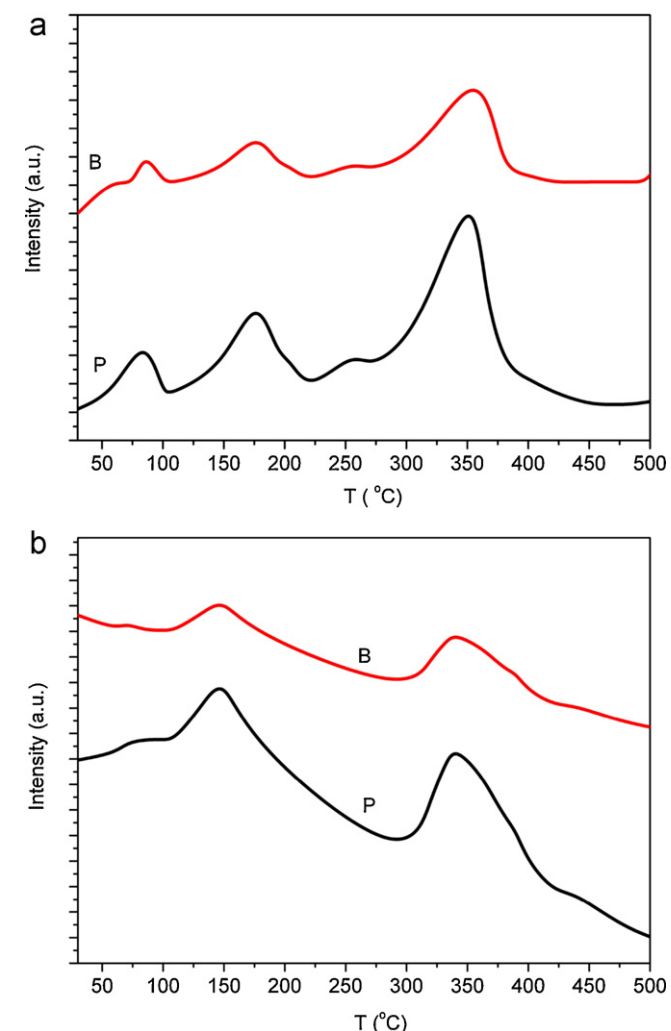


Fig. 11. CO adsorption behaviors of the  $\text{Co}_3\text{O}_4$  samples: (a) CO-TPD; (b)  $\text{CO}_2$ -TPD.

**Table 6**

The peak areas of CO and CO<sub>2</sub> desorbed from the catalysts.

| Sample | CO (a.u.) | CO <sub>2</sub> (a.u.) | Total area (a.u.) |
|--------|-----------|------------------------|-------------------|
| P      | 181.66    | 726.51                 | 909.17            |
| B      | 78.97     | 269.12                 | 348.09            |

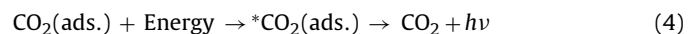
tion peaks of CO<sub>2</sub> at about 150 and 350 °C. The quantitative analysis results are summarized in Table 6. The total peak area (909.17 a.u.) of CO adsorbed on the porous Co<sub>3</sub>O<sub>4</sub> nanorods is much larger than that (348.09 a.u.) on the bulk one, indicating that there are more active sites on the former.

Fig. 12 shows the O<sub>2</sub>- and CH<sub>4</sub>-TPD profiles of the samples, and the desorption amounts of O<sub>2</sub> and CH<sub>4</sub> are summarized in Table 7. According to the literatures [40–43], the desorption peak of oxygen below 300 °C can be ascribed to the desorption of surface oxygen species, and the desorption peak above 300 °C is attributed

to the desorption of lattice oxygen. In Fig. 12a, the desorbed oxygen amount (85.1 vs. 82.1 μmol g<sup>-1</sup>) from the porous and the bulk samples are almost same above 300 °C; below 300 °C, the desorbed oxygen amount (18.4 μmol g<sup>-1</sup>) from the porous sample is larger than that (9.3 μmol g<sup>-1</sup>) from the bulk one. This indicates that there are more surface oxygen species on the porous nanorods. It is generally accepted that adsorbed surface oxygen species play a key role in CO oxidation [41]. In Fig. 12b, the desorption amounts of CH<sub>4</sub> from the porous and the bulk samples are 0.6 and 0.17 μmol g<sup>-1</sup>, respectively. Compared with the oxygen adsorption, the CH<sub>4</sub> adsorption on the catalyst is far weaker. This indicates that the combustion of CH<sub>4</sub> may proceed with the surface reaction between the gaseous CH<sub>4</sub> and the adsorbed or/and bulk oxygen [41,44].

#### 4. Discussion

It is generally accepted that the CTL luminescence results from the excited species produced in catalytic reaction [45]. The chemical reaction produces energy enough to induce the transition of electrons from the ground state to an excited electronic state. This electronic state transition is often accompanied by vibrational and rotational changes of the molecule. The CTL is observed when the electronically excited species decay to its ground state with the emission of photons. For CO oxidation, the CTL reaction can be represented with the following formula [46]:



It is accepted that CO<sub>2</sub> is the luminescence species. While CO molecules are oxidized on the catalyst surface, an amount of energy is released, which would be absorbed by CO<sub>2</sub> molecules. As a result, CO<sub>2</sub> molecules would jump from ground state up to electronic excited state (<sup>\*</sup>CO<sub>2</sub>). While the electronic excited <sup>\*</sup>CO<sub>2</sub> molecules decay to the ground state, a CTL signal is generated. The CTL spectra are closely correlated with the catalytic reaction, in which the conversion of CO to CO<sub>2</sub> is directly related to the catalytic properties of the catalysts. The easier the catalytic reaction is, the more CO<sub>2</sub> molecules are produced. As a result, the CTL intensity becomes stronger. Importantly, the activity order of the catalysts for CO oxidation is well consistent with that of the CTL intensity. It seems that the activity curve and the CTL spectrum represent the same catalytic reaction process. It is reasonable that the CTL mode can be an effective means to judge the catalyst activity, because the determination of the CTL spectra can be fulfilled within a few minutes.

For the CH<sub>4</sub> catalytic combustion, it is well known that at low conversions of CH<sub>4</sub>, combustion reaction is mainly controlled by surface reaction; at high conversions the oxidation of CH<sub>4</sub> involves surface reaction and free radical reaction [47]. The free radical reactions are more dependent on mass transfer than on the surface reaction. Because the surface reaction at high temperatures is fast relatively, the influence of mass transfer from the bulk gas to the catalyst surface on the combustion cannot be ignored. The surface reaction and mass transfer are affected by various factors, e.g., intrinsic activity, particle size and pore structure, etc. The highly porous structure and large surface area of the porous nanorods are beneficial to mass transfer [47]. As a result, the activity difference ( $\Delta T_{10} = 25^\circ\text{C}$ ) of the porous nanorods and the bulk Co<sub>3</sub>O<sub>4</sub> at GHSV = 48,000 h<sup>-1</sup> is same as that

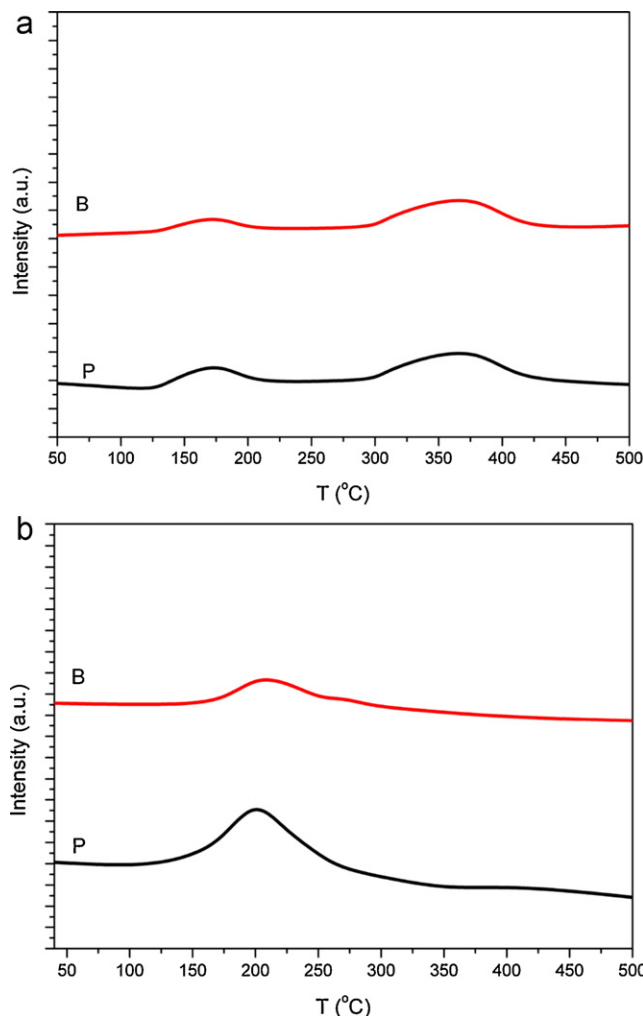


Fig. 12. O<sub>2</sub>-TPD (a) and CH<sub>4</sub>-TPD (b) profiles of the Co<sub>3</sub>O<sub>4</sub> samples.

**Table 7**

The peak areas of O<sub>2</sub> and CH<sub>4</sub> desorbed from the catalysts.

| Sample | Desorbed amount of O <sub>2</sub> (μmol g <sup>-1</sup> ) |         |              | Desorbed amount of CH <sub>4</sub> (μmol g <sup>-1</sup> ) |
|--------|---|---------|--------------|--|
|        | <300 °C   | >300 °C | Total amount |  |
| P      | 18.4  | 85.1    | 103.5        | 0.60   |
| B      | 9.3   | 82.1    | 91.4         | 0.17   |

( $\Delta T_{10} = 25^\circ\text{C}$ ) at GHSV = 100,000 h<sup>-1</sup>. However, the activity difference ( $\Delta T_{90} = 85^\circ\text{C}$ ) at GHSV = 100,000 h<sup>-1</sup> is significantly larger than that ( $\Delta T_{90} = 45^\circ\text{C}$ ) at GHSV = 48,000 h<sup>-1</sup>. Moreover, the reaction rates per square meter of both samples have been calculated and given in Fig. S8. It seems that at lower temperatures the reaction rates per square meter over both samples are similar; at higher temperatures the reaction rates per square meter over the bulk sample are larger than those over the porous sample. This may indicate that the number of active sites is not directly proportional to the BET area. Considering the high surface area of the porous nanorods, its total apparent reaction rate per gram is higher than that of the bulk sample. The similar results are reported in the literatures [34–37]. Further, we also investigate the stability of the porous nanorods by running the combustion reaction at 650 °C for 20 h under GHSV = 100,000 h<sup>-1</sup> (Fig. S9). The conversions of methane combustion are measured every 2 h. It shows that the combustion activity is maintained. After running for 20 h, the BET area of the porous nanorods is determined to be 164.3 m<sup>2</sup> g<sup>-1</sup> by nitrogen adsorption. Compared with the BET area (170.2 m<sup>2</sup> g<sup>-1</sup>) before running, the porous nanorods maintain its BET area considering that the measured value is within the analysis error ( $\pm 10\%$ ) of the method. For ordered mesoporous materials (e.g., MCM41 or SBA-15), their stabilities are limited by pore wall thickness and amorphous phase structure. Unlike ordered mesoporous materials, the porous nanorod sample shows a high stability since its pores result from the interstices among closely packed nanoparticles with high crystallinity. Besides, the spinel cobalt oxide is generally stable at the temperatures lower than 700 °C [48]. Therefore the porous nanorods show a high stability.

## 5. Conclusions

The highly porous Co<sub>3</sub>O<sub>4</sub> nanorods can be synthesized by a simple hydrothermal method, which have a narrow pore-size distribution and a high surface area. Compared with the bulk Co<sub>3</sub>O<sub>4</sub>, the porous Co<sub>3</sub>O<sub>4</sub> nanorods show a higher CTL intensity of CO oxidation and a higher catalytic activity of CH<sub>4</sub> combustion. Especially at a higher GHSV feed, the porous Co<sub>3</sub>O<sub>4</sub> nanorods show a higher activity for CH<sub>4</sub> combustion due to the higher surface area and the advanced porous structure. The highly porous Co<sub>3</sub>O<sub>4</sub> nanorods can be potentially used as the excellent catalyst at a high GHSV feed.

## Acknowledgments

This work is financially supported by National Science Foundation of China (20943004, 21177089), Six Talent Climax Foundation of Jiangsu (20100292), “333” Outstanding Youth Scientist Foundation (20110211) of Jiangsu, and National Science Foundation of China with Xinjiang (21173090).

## Appendix A. Supplementary data

Supplementary data associated with this article can be found, in the online version, at doi:10.1016/j.apcatb.2011.08.035.

## References

- [1] H.G. Yang, C.H. Sun, S.Z. Qiao, J. Zou, G. Liu, S.C. Smith, H.M. Cheng, G.Q. Lu, Nature 453 (2008) 639.
- [2] X. Xie, Y. Li, Z.-Q. Liu, M. Haruta, W. Shen, Nature 458 (2009) 746.
- [3] C.L. Cheung, A. Kurtz, H. Park, C.M. Lieber, J. Phys. Chem. B 106 (2002) 2429.
- [4] E. Kim, D. Son, T.G. Kim, J. Cho, B. Park, K.S. Ryu, S.H. Chang, Angew. Chem. 116 (2004) 6113.
- [5] Y. Wan, D.Y. Zhao, Chem. Rev. 107 (2007) 2821.
- [6] M.E. Davis, Nature 417 (2002) 813.
- [7] B. Varghese, T.C. Hoong, Y. Zhu, M.V. Reddy, B.V.R. Chowdari, Adv. Funct. Mater. 17 (2007) 1932.
- [8] X.W. Hou, D. Deng, J.Y. Lee, J. Feng, L.A. Archer, Adv. Mater. 20 (2008) 258.
- [9] C.C. Li, X.M. Yin, T.H. Wang, H.C. Zeng, Chem. Mater. 21 (2009) 4984.
- [10] K.T. Nam, D.W. Kim, P.J. Yoo, C.Y. Chiang, N. Meethong, P.T. Hammond, Y.M. Chiang, A.M. Belcher, Science 312 (2006) 885.
- [11] H. Zhang, J. Wu, C. Zhai, X. Ma, N. Du, J. Tu, D. Yang, Nanotechnology 19 (2008) 035711.
- [12] W.Y. Li, L.N. Xu, Chen, J. Adv. Funct. Mater. 15 (2005) 851.
- [13] F. Teng, W. Yao, Y. Zhu, G. Gao, D.D. Meng, J. Non-Cryst. Solids 355 (2009) 2375.
- [14] L. Li, Y. Chu, Y. Liu, J. Song, D. Wang, X. Du, Mater. Lett. 62 (2008) 1507.
- [15] J. Feng, H.C. Zeng, Chem. Mater. 15 (2003) 2829.
- [16] T. He, D.R. Chen, X.L. Jiao, Y.L. Wang, Adv. Mater. 18 (2006) 1078.
- [17] T. Yu, Y.W. Zhu, X. Xu, Z. Shen, P. Chen, C.T. Lim, J.T.L. Thong, C.H. Sow, Adv. Mater. 17 (2005) 1595.
- [18] Y. Lu, Y. Wang, Y. Zou, Z. Jiao, B. Zhao, Y. He, M. Wu, Electrochim. Commun. 12 (2010) 101.
- [19] S. Xiong, C. Yuan, X. Zhang, B. Xi, Y. Qian, Chem. Eur. J. 15 (2009) 5320.
- [20] C. Ma, Z. Mu, J. Li, Y. Jin, J. Cheng, G.Q. Lu, Z. Hao, S. Qiao, J. Am. Chem. Soc. 132 (2010) 2608.
- [21] B.Z. Tian, X. Liu, L. Solovyov, Z. Liu, H. Zang, Z. Zhang, S. Xie, F. Zhang, B. Tu, C. Yu, O. Terasaki, D. Zhao, J. Am. Chem. Soc. 126 (2004) 865.
- [22] Y.Q. Wang, C.M. Yang, W.G. Schmidt, B. Spiethoff, E. Bill, F. Schuth, Adv. Mater. 17 (2005) 53.
- [23] H. Tüysüz, Y. Liu, C. Weidenthaler, F. Schüth, J. Am. Chem. Soc. 130 (2008) 14108.
- [24] R. Xu, J. Wang, Q. Li, G. Sun, E. Wang, S. Li, J. Gu, M. Ju, J. Solid State Chem. 182 (2009) 3177.
- [25] G. Binotto, D. Larcher, A.S. Prakash, R.H. Urbina, M.S. Hegde, J.-M. Tarascon, Chem. Mater. 19 (2007) 3032.
- [26] S.H. Lee, T.W. Kim, D.H. Park, J.H. Choy, S.-J. Hwang, Chem. Mater. 19 (2007) 5010.
- [27] J. Liu, H. Xia, L. Lu, D. Xue, J. Mater. Chem. 20 (2010) 1506.
- [28] H. Cölfen, S. Mann, Angew. Chem., Int. Ed. 42 (2003) 2350.
- [29] L. Ren, P. Wang, Y. Han, C. Hu, B. Wei, Chem. Phys. Lett. 476 (2009) 78.
- [30] J. Zheng, W. Chu, H. Zhang, C. Jiang, X. Dai, J. Nat. Gas Chem. 19 (2010) 583.
- [31] Y.F. Zhu, J. Shi, Z. Zhang, C. Zhang, X.R. Zhang, Anal. Chem. 74 (2002) 120.
- [32] V.G. Hadjiev, M.N. Iliev, I.V. Vergilov, J. Phys. C: Solid State Phys. 21 (1988) L199.
- [33] K.S.W. Sing, D.H. Everett, R.A.W. Haul, L. Moscou, R.A. Pierotti, J. Rouquerol, T. Siemieniewska, Pure Appl. Chem. 57 (1985) 603.
- [34] J. Kirchnerova, M. Alifanti, B. Delmon, Appl. Catal. A: Gen. 231 (2002) 65.
- [35] L.F. Liotta, G. Di Carlo, G. Pantaleo, G. Deganello, Catal. Commun. 6 (2005) 329.
- [36] L.F. Liotta, G. Di Carlo, A. Longo, G. Pantaleo, A.M. Venezia, Catal. Today 139 (2008) 174.
- [37] N. Bahlawane, Appl. Catal. B: Environ. 67 (2006) 168.
- [38] J. Liu, D. Xue, Adv. Mater. 20 (2008) 2622.
- [39] P.G. Harrison, I.K. Ball, W. Daniell, P. Lukinskas, M. Cespedes, E.E. Miro, M.A. Ulla, Chem. Eng. J. 95 (2003) 47.
- [40] N. Bahlawane, E.F. Rivera, K.K. Hoinghaus, A. Brechling, U. Kleineberg, Appl. Catal. B 53 (2004) 245.
- [41] L. Xue, C. Zhang, H. He, Y. Teraoka, Appl. Catal. B 75 (2007) 167.
- [42] Z.P. Hao, D.Y. Cheng, Y. Guo, Y.H. Liang, Appl. Catal. B 33 (2001) 217.
- [43] Y. Yu, T. Takei, H. Ohashi, H. He, X. Zhang, M. Haruta, J. Catal. 267 (2009) 121.
- [44] M.J. Pollard, B.A. Weinstock, T.E. Bitterwolf, P.R. Griffiths, A.P. Newbery, J.B. Paine, J. Catal. 254 (2008) 218.
- [45] L. Marchetti, L. Forni, Appl. Catal. B 15 (1998) 179.
- [46] X. Wang, N. Na, S. Zhang, Y. Wu, X. Zhang, J. Am. Chem. Soc. 129 (2007) 6062.
- [47] X.Y. Huang, J.C. Ren, Trends Anal. Chem. 25 (2006) 155.
- [48] L.F. Liotta, G. Di Carlo, G. Pantaleo, A.M. Venezia, G. Deganello, Appl. Catal. B: Environ. 66 (2006) 217.